Full length article

In situ characterization of work hardening and springback in grade 2 α-titanium under tensile load

K. Sofinowski [a,b], M. Šmíd [a], S. van Petegem [a], S. Rahimi [c], T. Connolley [d], H. van Swygenhoven [a,b,*]

[a] *Photons and Engineering for Manufacturing, Paul Scherrer Institut, CH-5232 Villigen, Switzerland*
[b] *Neutrons and X-rays for Mechanics of Materials, IMX, École Polytechnique Fédérale de Lausanne, CH-1012 Lausanne, Switzerland*
[c] *Advanced Forming Research Centre, University of Strathclyde, 85 Inchinnan Drive, Glasgow PA4 9LJ, UK*
[d] *Diamond Light Source Ltd., Harwell Science and Innovation Campus, Didcot, Oxfordshire OX11 0DE, UK*

ARTICLE INFO

ABSTRACT

Plastic effects during sheet metal forming can lead to undesirable distortions in formed components. Here, the three-stage work hardening and plastic strain recovery ("springback") in a cold-rolled, α-phase commercially pure titanium is examined. Interrupted standard tensile tests with *in situ* x-ray diffraction and quasi-*in situ* electron backscatter diffraction show that twinning plays a minor role in both of these phenomena. The experiments give evidence that the observed work hardening plateau is the result of an abrupt activation and multiplication of $\langle c + a \rangle$ slip and a subsequent redistribution of load between grain families. The springback can be attributed to inelastic backwards motion and annihilation of dislocations, driven by backstresses from dislocation-based hardening during loading. The peak broadening behavior, observed by x-ray diffraction, suggests that the internal stress state is highest in the rolling direction, resulting in consistently higher springback magnitude along this direction.

© 2019 Acta Materialia Inc. Published by Elsevier Ltd.
This is an open access article under the CC BY-NC-ND license.
(http://creativecommons.org/licenses/by-nc-nd/4.0/)

1. Introduction

Commercially pure Ti (CP-Ti) exhibits strong anisotropic behavior as a result of its hexagonal close-packed structure. This results in micromechanical effects such as multi-stage work hardening [1–3] and plastic strain recovery during unloading ("springback") [4–6]. These effects cause cold-formed parts to deviate from their desired profile and higher-than-predicted residual stresses following the deformation [7].

Recently, Khayatzadeh et al. [8,9] reported that the springback in a Grade 2 CP-Ti shows a non-linear anelastic recovery during unload. Similar non-linear springback effects have been previously observed in a wide range of steels [7,10–18] and is known to vary with the alloy composition. However, most of the existing studies are focused on fitting constitutive models, and only a few attempts have been made to explain the underlying microstructural mechanisms of the effect. Luo and Ghosh [7] suggest that the bowback of pinned dislocations and disintegration of dislocation cell structures

generated during deformation contribute to the non-linear springback in drawing quality specially killed (DQSK) steel. Post-mortem TEM observations in pure Fe by Benito et al. [12] support this description.

As compared to steels and other FCC alloys, characterization of springback in HCP alloys is considerably less developed. Due to the inherent anisotropy of the HCP unit cell, additional deformation behaviors must be taken into account. It has been observed, for example, that deformation in α-phase Ti polycrystals is dominated by single slip [19,20] and do not form dislocation cells, implying that different mechanisms than those described above for steel [7] must be active. Without five easily-activated independent slip systems, deformation twinning is often observed in HCP metals. Cáceres et al. [21] attributed the anelastic springback in AZ91 magnesium to partial reversal of tension twins formed during loading. Additionally, $\{10.2\}\langle 10.1\rangle$ tension twinning in CP-Ti causes an $84.8°$ rotation of the unit cell [1,2], resulting in significant texture changes during loading. Hama et al. [22] showed in a magnesium alloy that plastically hard grains twinned into plastically soft orientations, leading to increased easy glide of dislocations during unloading that contributed to additional strain recovery. Even in the absence of twinning, Abdolvand et al. [23] observed that

* Corresponding author at: Photons and Engineering for Manufacturing, Paul Scherrer Institut, CH-5232 Villigen, Switzerland.
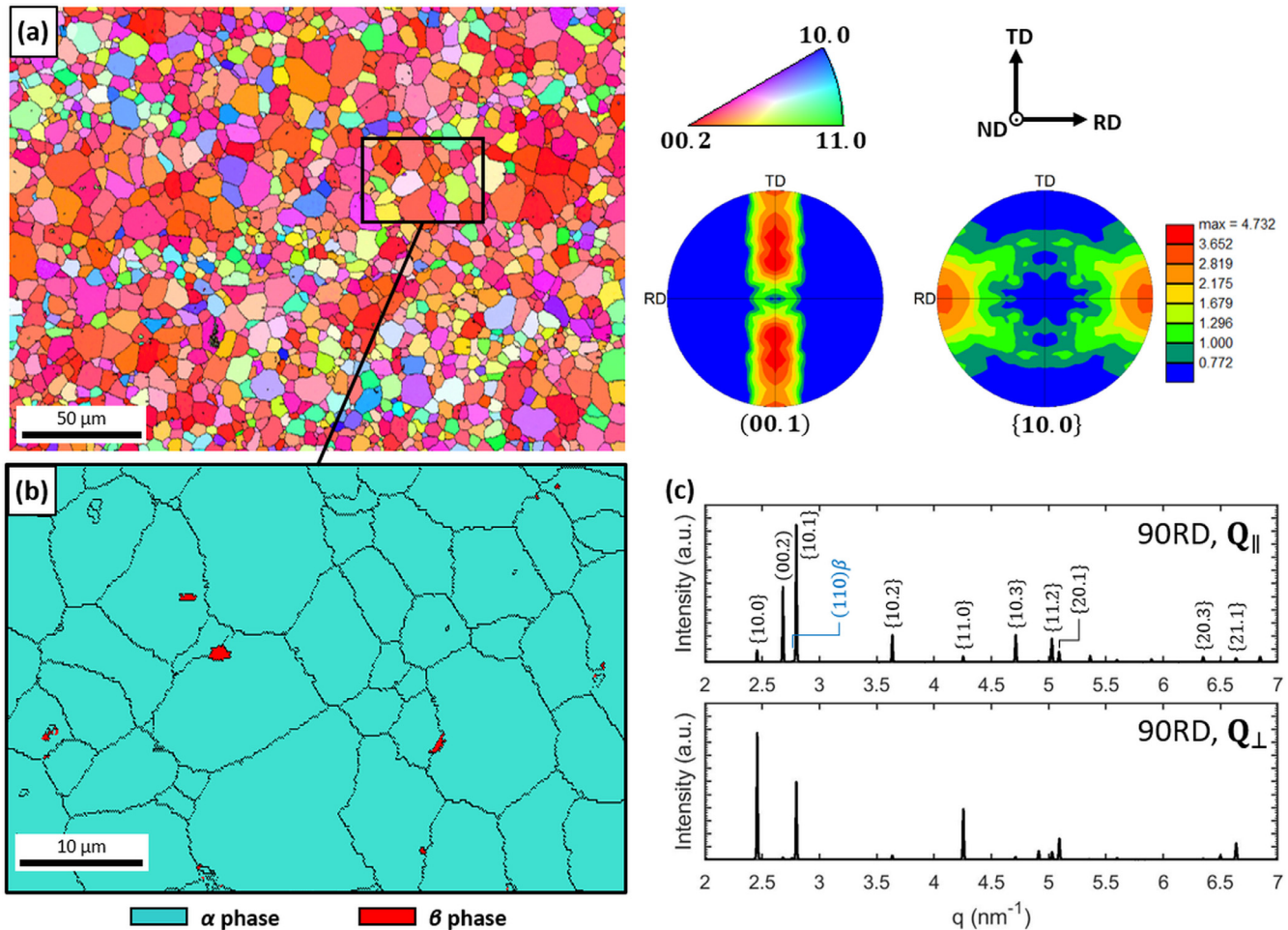*E-mail address:* helena.vs@psi.ch (H. van Swygenhoven).

Fig. 1. Initial microstructure of CP-Ti: (a) IPF grain orientation map with respect to TD (90° to RD) with 0001 and 10$\bar{1}$0 pole figures; (b) Magnified section of the corresponding phase map showing a few β grains in red; (c) Undeformed axial ($\mathbf{Q}_{\parallel}$) and radial ($\mathbf{Q}_{\perp}$) XRD patterns.

intergranular stresses on certain grains in CP-Ti could decrease during continuous tensile loading depending on their grain neighborhood. Thus, the microstructural sources of springback in CP-Ti warrant further investigation.

Additionally, the stress–strain behavior of the CP-Ti studied by Khayatzadeh et al. [8,9] showed distinct three-stage work hardening during loading in tension. This behavior is often described during compression for CP-Ti [24–28] and other HCP materials [29–32] as the result of {10.2}⟨10.1⟩ tension twinning and the subsequent hardening as dislocation glide is hindered by the new twin boundaries. More recently, the three-stage work hardening has been reported for tension tests in CP-Ti [1–3]. Becker and Pantleon [2] reported that the three stages A, B, and C correspond to easy dislocation slip, the activation of {11.2}⟨$\bar{1}\bar{1}$.3⟩ compression twinning, and the saturation of this twinning system and subsequent activation of {10.2}⟨10.1⟩ tension twinning. On the other hand, Roth et al. [1] observed almost no twinning (<0.5% and 5.7 vol%. fraction for rolling direction and transverse direction samples, respectively) and thus proposed that the work hardening plateau is related primarily to dislocation-based plasticity.

This study examines the three-stage work hardening and nonlinear springback in the Grade 2 CP-Ti. Interrupted tensile tests are performed with *in situ* high-energy x-ray diffraction (XRD) to examine the development of intergranular stresses during loading and unloading. The twin volume and growth is quantified by quasi-*in situ* electron backscatter diffraction (EBSD). A description of each effect is proposed based on the XRD and EBSD results.

2. Experimental procedure

2.1. Material

Sheets of commercially pure titanium (CP-Ti Grade 2) cold-rolled to 1.6 mm thick were supplied by TIMET. The initial microstructure is shown in Fig. 1. The grain orientations are shown with respect to the loading direction, 90° to RD (Fig. 1(a)). The material exhibits a slight basal texture perpendicular to RD typical of cold-rolled Ti. The CP-Ti is >99.8% α phase with small retained β grains dispersed throughout the material, as seen in the magnified section of the phase map in Fig. 1(b). The α grains are generally equiaxed with a grain size of 8.2 ± 3.4 μm while the β grains have a grain size of 0.7 ± 0.4 μm. The texture of the α grains is also visible in the axial ($Q_{\parallel}$) and radial ($Q_{\perp}$) diffraction patterns of the undeformed samples (Fig. 1(c)).

2.2. In situ x-ray diffraction (XRD)

Flat, dogbone-shaped specimens were cut from the sheet using electrical discharge machining (EDM) at 0°, 45°, and 90° to the rolling direction (RD). The specimen design was based on the ASTM E8/EM8-11 test standard scaled so that the reduced section length was 32 mm. Interrupted uniaxial tensile tests were performed *in situ* using an INSTRON 100 kN tensile test rig integrated into the XRD facilities. Samples were loaded using displacement control to 3.5%, 7%, and 10.5% total strain (3.5%, 5.25%, and 7% for

Table 1
Literature data for CRSS values relative to $CRSS_{Pri\langle a \rangle}$ for commercial purity Ti at room temperature.

Model [Ref.]	CRSS (MPa)	Relative CRSS (MPa)			
	$Pri\langle a \rangle$	$Ba\langle a \rangle$	$Pyr\langle a \rangle$	$Pyr^{1st}\langle c + a \rangle$	$Pyr^{2nd}\langle c + a \rangle$
TEM + Slip trace analysis [40]	120	1.5	1.2	2.0	–
CPFE single crystal [41]	181	1.2	–	2.6	–
CPFE single crystal [42]	150	2.3	–	7.4	–
Taylor-type modeling [43]	–	6.0	–	9.0	–
VPSC [44]	90	2.5	–	9.4	–
EPSC [45]	80	1.1	1.4	3.3	–
VPSC [46]	57	4.8	2.9	5.4	4.1
EPSC [47]	68	2.6	1.8	3.7	–
EVPSC [3]	141	1.8	1.4	2.4	2.5
EVPSC [48]	50	2.4	1.8	1.3	3.0

the samples at 90° to RD, due to the lower ductility along this direction) and unloaded to 20 MPa using force control. After each unloading step, the sample was held constant at 20 MPa for five minutes before reloading. Mechanical data was collected at a sampling rate of 94 Hz. The samples were loaded with an initial strain rate of $\dot{\varepsilon} = 0.0001$ s^{-1} and unloaded in force control at a rate of $dF/dt = -4$ N/s. The slow loading and unloading rates were chosen to give time to capture XRD spectra, as previous research on this material [9] suggests that the springback is largely independent of strain rate. Three samples were tested for each test type to ensure consistency in the measured results.

High energy XRD was performed during interrupted tensile tests at the JEEP I-12 beamline at Diamond Light Source, UK [33]. Samples were measured in transmission using a 53 keV beam with 300 × 300 μm^2 spot size. Diffraction patterns were recorded over 8 s intervals with a Pilatus 2M CdTe 2D area detector. The 2D images were radially binned using DAWN XRD processing software [34] at ± 3° parallel and perpendicular to the tensile axis ($Q_{\parallel}$ and $Q_{\perp}$, respectively). Samples are mounted such that the $Q_{\parallel}$ signal measures along the loading direction while the $Q_{\perp}$ signal measures the transverse direction, in-plane with the sheet.

The diffraction peaks were fit using a split Pearson VII function to extract the peak position $\theta_{hk.l}$, peak width (full-width at half-maximum, $\beta(2\theta_{hk.l})$), and integrated intensity. The elastic lattice strains for a given grain family were calculated from the change in peak position of the corresponding $\{hk.l\}$ reflection ($\varepsilon_{hk.l} = -\pi \cot(\theta_{hk.l})(\theta_{hk.l} - \theta^0_{hk.l})/360$) and used to examine how the applied load is shared between different grain families (e.g. [35–38]). In the elastic regime, the elastic lattice strain evolves linearly with the applied stress. As grain families begin to deform plastically, the load is transferred between the grains and $\varepsilon_{hk.l}$ deviates from linearity. For the $Q_{\parallel}$ (axial) reflections, an increase in $\varepsilon_{hk.l}$ means that the grain family goes in tension while a decrease means that it goes into compression along the tensile axis. For the $Q_{\perp}$ (radial) reflections, the change in $\varepsilon_{hk.l}$ is measured perpendicular to the loading direction, i.e. the Poisson contraction is measured. Thus an increase in $\varepsilon_{hk.l}$ implies that the grain family is in compression and vice versa.

2.2.1. Schmid factor (SF) analysis

Schmid factors were calculated for all deformation mechanisms according to a generalized Schmid law proposed by Muránsky et al. [35]:

$$\mathbf{m} = \mathbf{b} \cdot \mathbf{g} \cdot \mathbf{S} \cdot \mathbf{g^T} \cdot \mathbf{n^T} \tag{1}$$

where $\mathbf{b}$ is the Burgers vector for slip, $\mathbf{S}$ is the 3-D stress tensor (in this case, the uniaxial stress), and $\mathbf{n}$ is the normal to the slip plane. For twinning, $\mathbf{b}$ and $\mathbf{n}$ are the twinning direction and normal to the twinning plane, respectively. The matrix $\mathbf{g}$ is a rotation matrix relating the stress tensor and grain orientation. Each axial grain family was converted to an orthonormal basis and the SFs for

all possible slip systems were calculated using a c/a ratio of 1.588. The axial inverse pole figures (IPFs) of the maximum SF under uniaxial tension are shown in Fig. 2. The IPFs are generated using the texture analysis toolbox MTEX developed in MATLAB^{TM} [39].

Critical resolved shear stress (CRSS) values from literature for commercially purity α-Ti at room temperature are shown in Table 1. It is generally agreed upon that $\langle a \rangle$ slip on prismatic planes ($Pri\langle a \rangle$) is considered the easiest deformation mechanism. There is less consensus on the relative strengths of other mechanisms. The results of most recent crystal plasticity modeling suggest that pyramidal $\langle a \rangle$ slip ($Pyr\langle a \rangle$) is the second easiest and basal $\langle a \rangle$ slip ($Ba\langle a \rangle$) the third. It should be noted, however, that $Pyr\langle a \rangle$ slip is rarely directly observed by microscopy. $Ba\langle a \rangle$ slip is readily observed and the CRSS varies strongly with interstitial content. Conrad [49] reported that the ratio between the CRSS of $Ba\langle a \rangle$ and $Pri\langle a \rangle$ slip varies strongly with oxygen content, from ~9 × to ~1.2 × between 0 and 0.23 wt% oxygen. This can explain the larger values of 6 × and 4.8 × reported by Philippe et al. [43] and Benmhenni et al. [46] in Table 1, respectively, as they examined Ti with 0.11 wt% and 0.12–0.14 wt% oxygen. However, Warwick et al. [45] report a $Ba\langle a \rangle/Pyr\langle a \rangle$ slip CRSS ratio of 1.1 × on a Ti with 0.07 wt% oxygen, so it is clear that other elements play a role. In general, the CRSS of $Ba\langle a \rangle$ slip appears to be ~1.2–2.6 × higher than $Pri\langle a \rangle$ slip in commercial purity Ti.

Except for the recent work of Richeton et al. [48], $\langle c + a \rangle$ slip is generally regarded as more difficult than $\langle a \rangle$ slip mechanisms, which can result in twinning to accommodate strain along the c-axis. Slip along first-order pyramidal planes ($Pyr^{1st}\langle c + a \rangle$) is the main slip mechanism for accommodating strain along the c-axis. Slip along second-order pyramidal planes is not commonly reported, although it has been observed by Xiaoli et al. [50] in a high purity Ti single crystal.

In combination with the CRSS, the SF can be used to identify the predominant active deformation mechanisms in a grain family at the onset of plasticity. This approach is not necessarily valid for individual grains in polycrystals or at high plastic strains, as it has been shown that the local stress tensor can differ significantly from the applied stress tensor (e.g. [23]). However, on a grain family scale, this approach has been shown to be a good predictor of active plasticity mechanisms at low strains [35,36].

2.2.2. Williamson–Hall plots

The peak broadening ($\beta(2\theta_{hk.l})$) of an XRD peak is the convolution of both a size broadening and strain broadening. The size broadening is due to the finite coherent scattering volume of the diffracting grains. The strain broadening is due to the presence of inhomogeneous strain within the crystallites, which causes the lattice spacing $d_{hk.l}$ of the grains to deviate locally from the average lattice spacing. Inhomogeneous strain is caused by distortions in the crystal lattice and can thus provide information on how dislocations are accumulating in the grains [51].
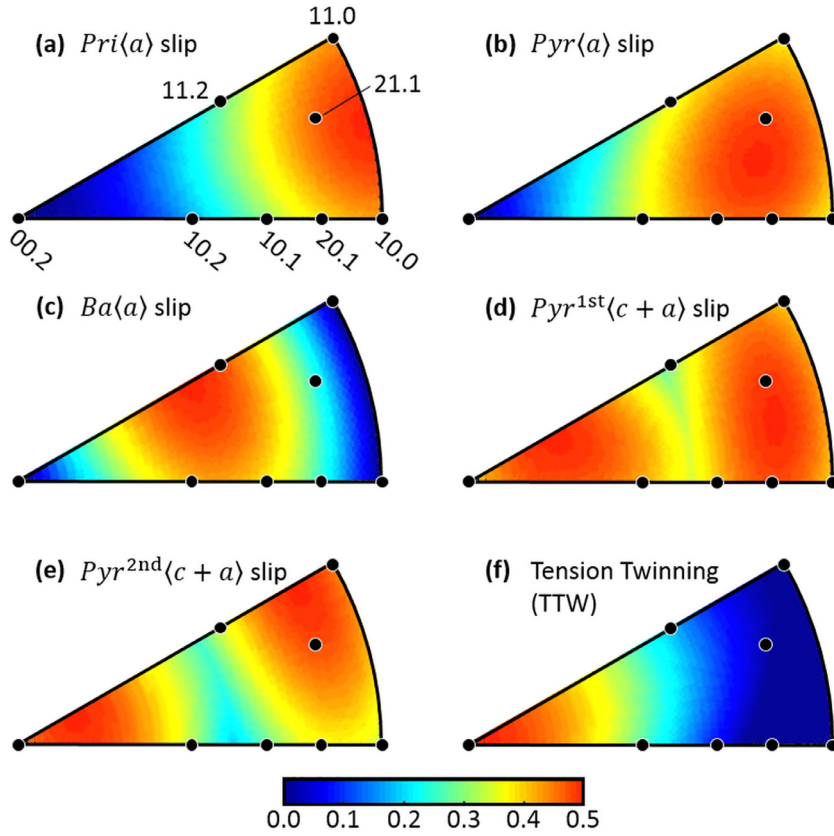
Fig. 2. Axial ($\mathbf{Q}_{\parallel}$) inverse pole figures of the maximum SF under uniaxial tension for all probable deformation mechanisms in Ti. Grain family plane normal are defined parallel to the loading direction.

The size and strain broadening contributions each exhibit a different dependence on the Bragg diffraction angle $\theta_{hk.l}$. The size broadening is given by the Scherrer equation [52]:

$$\beta_{\text{size}} = \frac{K\lambda}{D\cos(\theta_{hk.l})} \qquad (2)$$

where K is a constant related to the shape of the grains, λ is the x-ray wavelength, D is the mean size of the coherent scattering volume, and $\theta_{hk.l}$ is the Bragg angle. As a rule of thumb, the size broadening is indistinguishable from the instrumental broadening for coherent scattering lengths above 1 μm, so it is not expected to play a large role in this study. The strain broadening can be described by [53]:

$$\beta_{\text{strain}} = 4e\tan(\theta_{hk.l}) \qquad (3)$$

where e is an upper limit approximation for the strain in the diffracting crystallites. The total peak broadening is the convolution of these two terms. The peaks in this study are well-described by a Lorentzian peak profile, so we make the simplifying assumption that the two components can be represented by Lorentzian peak shapes. The convolution then simplifies to the sum of the size and strain components:

$$\beta(2\theta_{hk.l}) = \beta_{\text{size}} + \beta_{\text{strain}} \qquad (4)$$

and by defining a variable $s \equiv 2\sin(\theta_{hk.l})/\lambda$ and substituting Eqs. (2) and (3) into Eq. (4) results in:

$$\beta(2\theta_{hk.l}) = \frac{K}{D} + 2es \qquad (4)$$

Thus, the size broadening does not depend on the variable s, while the strain broadening varies with it linearly.

Plotting this relationship for various grain families gives what is known as a Williamson–Hall plot (W–H plot) [54]. In a perfect polycrystal with no inhomogeneous strain, the grain families would fall on a straight line with a slope of 0 and an intercept related to the size broadening and instrumental broadening from the geometric limitations of the diffractometer. An increase in the slope of this regression line implies that the amount of inhomogeneous strain is increasing, *e.g.* by plastic deformation. The deviation above or below the regression line for each individual grain family gives information on how that family broadens in comparison to the "mean" broadening of all of the measured grains.

It should be noted that this broadening is also affected by the average contrast factor $\bar{C}$ of the grain family, *i.e.* how the active slip systems contribute to the peak broadening. Dragomir and Ungár [55] have shown that $\bar{C}$ varies non-linearly with the index of the *hk.l* peak reflection, and this variation depends on the active slip mechanisms and nature of the dislocations present (edge or screw). Thus, it is difficult to compare the broadening between grain families without significant assumptions of the dislocation activity in each grain family. Ungár and co-workers [56,57] attempted to address this by using a modified Williamson–Hall approach which factors in the contrast factor. However, they apply it to FCC metals, for which it is simple to assume the active slip mechanisms. The elastic anisotropy and heavily orientation-dependent slip mechanisms make it difficult to assume one contrast factor for a grain family, especially after the activation of multiple slip.

Whole peak profile fitting methods, such as the software CMWP (Convolution Multiple Whole Profile), in combination with programs such as Hexburger can be used to extract the relative
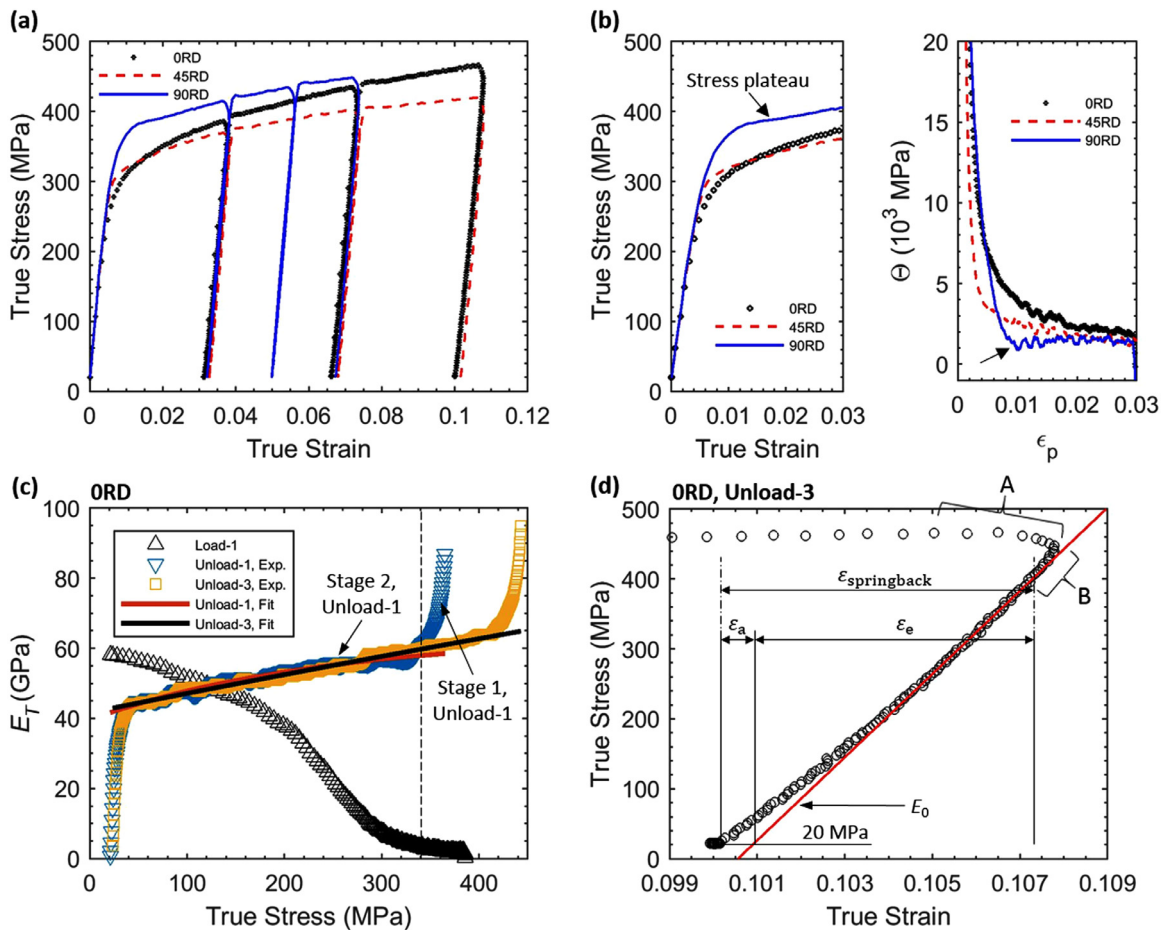
Fig. 3. (a) True stress–true strain response for samples loaded at 0°, 45°, and 90° to the rolling direction (0RD, 45RD, and 90RD); (b) Magnified view of the true stress–true strain curves for the first 3% of strain and the corresponding plastic work hardening rate Θ; (c) Instantaneous tangent modulus E_T versus true stress for the first load and first and last unload for the 0RD sample; (d) Magnified view of the final unload of the 0RD sample showing the springback and its components.

activity of deformation mechanisms in each grain family. These methods were applied to our samples. However, the Hexburger software was unable to define a suitable combination of deformation mechanisms to describe the broadening. Thus, Williamson Hall plots were used to avoid making assumptions about the active deformation mechanisms.

2.3. Quasi-in situ electron backscatter diffraction (EBSD)

Flat, dogbone-shaped specimens were cut from the sheet by EDM at 0°, 45°, and 90° to the RD. The specimen shape was the same as the large dog bone design in [58] but with a thickness of 1.6 mm. The samples were mechanically ground using silicon carbide grinding paper to 2400 grit, then polished with 6, 3, and 1 µm diamond paste for three minutes each. Final polishing was done with 0.05 µm high purity OPS colloidal silica solution for two sessions of 30 min each. Samples were then vibration-polished for 12 h to a mirror-finished condition for EBSD acquisition.

Interrupted uniaxial tensile tests were performed using an uniaxial tensile test rig (for details, see [58]). Samples were loaded using displacement control to 3.5% and 7% total strain and unloaded with a strain rate of $\dot{\varepsilon} = 0.0001$ s^{-1}. After each unload, the sample was removed and observed in a Zeiss ULTRA 55 field emission gun scanning electron microscope (FEG SEM) with an EDAX Hikari Camera. Images were captured at 20 kV in high current mode with an aperture of 120 µm. EBSD mapping was performed with 90 nm step size covering an area of 52×42 µm^2. The EBSD data was analyzed using OIM Analysis 7.3 software.

3. Results

3.1. Mechanical response

The macroscopic true stress–true strain response for test A for samples loaded at 0°, 45°, and 90° to the rolling direction (0RD, 45RD, and 90RD) are shown in Fig. 3(a). A slope change is visible in the stress–strain curve of the 90RD sample just after 0.2% yield (R$_{p0.2}$), highlighted in Fig. 3(b). The plastic work hardening rate $\Theta = d\sigma/d\varepsilon_p$ is plotted next to it as a function of plastic strain ε_p. It is clear in Fig. 3(b) that the 90RD curve shows three distinct work hardening phases: a strong initial decrease, a slight increase, then a slow decrease parallel with the 0RD and 45RD samples. Kayatzadeh et al. [9] observed the same three-stage hardening in this material at higher strain rates ($\dot{\varepsilon} = 0.002$, 0.01, and 0.1 s^{-1}) for all loading directions. At these higher strain rates, the stress drops (a negative slope of the stress–strain curve) before increasing again, and the magnitude of the drop decreases with decreasing strain rate and decreasing angle to the rolling direction. The low strain rate used in this study ($\dot{\varepsilon} = 0.0001$ s^{-1}) explains why the behavior is not observed for the 0RD and 45RD samples.

For all samples, the true stress–true strain curves deviate from linearity during both loading and unloading. Thus, to describe the loading and unloading behavior, the instantaneous tangent modulus E_T is calculated using a least squares fit over subsequent sets of 500 true stress–true strain data points. A similar procedure was used by Luo and Ghosh [7] to characterize the non-linear loading and unloading response of a DQSK steel. Fig. 3(c) shows E_T as
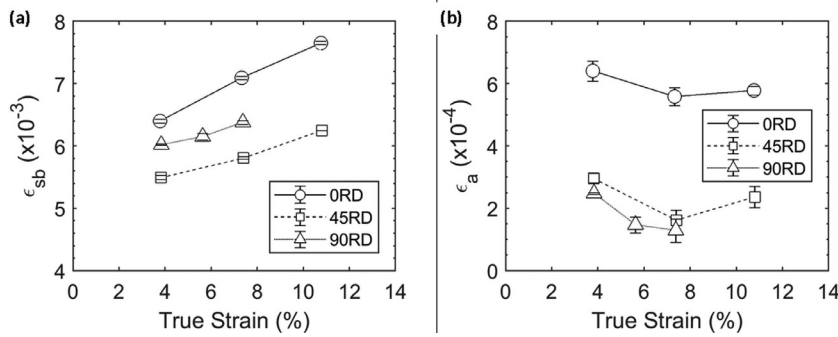
Fig. 4. Magnitude of springback for each dogbone: (a) total springback ε_{sb} and (b) anelastic component ε_{a} of the springback. The values are averaged over the three samples for each loading direction.

a function of true stress during initial loading and the first and last unloading stages for one of the 0RD samples. The consistent decrease in E_T during the loading and unloading shows that the curves are non-linear over the entire regime. However, it must be mentioned that the initial value of the modulus during loading is ~60 GPa, well below the reported modulus of 90–110 GPa [9]. This is a result of the compliance of the tensile test rig, as the strain is calculated by the displacement of the grips. As the purpose of this study is to examine the relative springback with respect to loading direction and prestrain, the magnitude of the modulus is not critical, but the trends of the springback are. An assumption must be made that the response of the machine is consistent for all tests. This is a reasonable assumption considering that the tests never exceed 5 kN of applied load, an order of magnitude lower than the machine limit of 100 kN.

During the unloading stages, E_T initially drops sharply with applied stress before leveling off to a more steady decrease (Fig. 3(c)). The initial drop is related to two behaviors. The first is the transition from displacement-controlled loading to force-controlled unloading. At the early stages of unloading the sample relaxes faster than the prescribed −4 N/s unload rate. This is compensated by continuous forward motion of the crosshead until the desired unload rate is met. This regime is marked "A" in Fig. 3(d), which shows the unloading of a 0RD sample after 10.5% straining (i.e. third unloading stage). The continued forward motion results in the real true strain reaching ~10.8% before the direction of the strain reverses. The second is a brief period of continued forward microplastic strain that delays how quickly the sample reaches the imposed unload rate. This has been previously described for DQSK steels [7]. In combination with the changing crosshead speed, this results in the non-linear E_T evolution, marked "B" in Fig. 3(d), before a steady unloading rate of −4 N/s is reached.

The evolution of E_T must therefore be divided into two stages: Stage 1, where the mechanical behavior is heavily influenced by the continuously changing crosshead speed, and Stage 2, where the reduction of E_T is primarily due to microstructural changes. The evolution of E_T in Stage 2 is non-linear and can be well-described by a function of the form $a(1 - e^{bx})$, which has no physical meaning but describes well the slow degradation in E_T during unloading. The transition between these two stages can then be defined as the stress at which the measured E_T deviates more than 5% from the fit to Stage 2 (Fig. 3(c)).

Due to the non-linear behavior of the unloading, it is inappropriate to define a linear "degraded elastic modulus," as is often done when calculating springback. Instead, the springback is split into an elastic and an anelastic component, ε_e and ε_a, respectively. The anelastic component is taken as the difference between the unloaded strain (at 20 MPa) and the total springback minus the initial elastic modulus E_0, and is related to all springback not associated with the elastic unload. Both components are shown

graphically in Fig. 3(d). The total springback, ε_{sb}, is calculated as the difference between the true strain at the end of Stage 1 and the end of unloading.

The magnitude of ε_{sb} and ε_a are shown in Fig. 4(a) and (b), respectively, for each loading direction. Three samples were measured for each loading direction, and the values shown in Fig. 4 are averaged over these values. One of the 90RD samples was loaded to different strain values for the third load and was therefore not included in the calculation. As expected, ε_{sb} increases with increasing macroscopic strain for all loading directions. The springback for 0RD is consistently higher than 45RD and 90RD. As with ε_{sb}, the magnitude of the anelastic springback ε_a is highest in 0RD but does not show any trends with increasing prestrain. These trends are consistent with those observed by Khayatzadeh et al. [9] for the same material at higher strain rates.

3.2. Quasi-in situ EBSD

Quasi-*in situ* EBSD was performed to examine the role of deformation twinning. The microstructures of the 0RD and 90RD samples in the unloaded state and after straining to 3.5% and 7% are shown in Fig. 5. In both samples, deformation twins are observed to form during the first loading cycle to $\varepsilon = 3.5\%$. During the second loading cycle to $\varepsilon = 7.0\%$, no new twins are formed, but existing twins tend to grow. In the 0RD sample, narrow $\{10.1\}\langle10.2\rangle$ compression twins are observed, whereas in the 90RD sample the observed twins are $\{10.2\}\langle10.1\rangle$ tension type. However, very little twinning is observed for both orientations. The area volume fraction of twins after 7% strain is 0.01% and 0.34% for 0RD and 90RD, respectively. By contrast, orientation gradients appear in many of the grains due to grain rotation caused by dislocation slip. The average grain size, however, does not appear to change significantly in this strain range.

3.3. In situ XRD

3.3.1. Peak evolution during tensile loading

The evolution of the axial ($Q_{\parallel}$) and radial ($Q_{\perp}$) α elastic lattice strains during the first load–unload cycle (to 3.5% strain) is shown in Fig. 6 as a function of the applied stress. The residual lattice strains after unloading are marked by "x". The initial lattice strain (at 20 MPa) of each grain family is not shown for clarity. For each grain family, a linear curve was fitted to the points in the elastic regime (under 180 MPa) and the lattice strains are shifted such that the fit passes through the initial point (20 MPa). A small but non-zero $(110)_{\parallel}$ β peak was observed in all samples. The behavior of the $(110)_{\parallel}$ β peaks was consistent for all loading directions. However, the fraction of β phase was measured by EBSD to be below 0.2%, so it is not expected to play a major role in the deformation. The elastic lattice strain evolution and peak
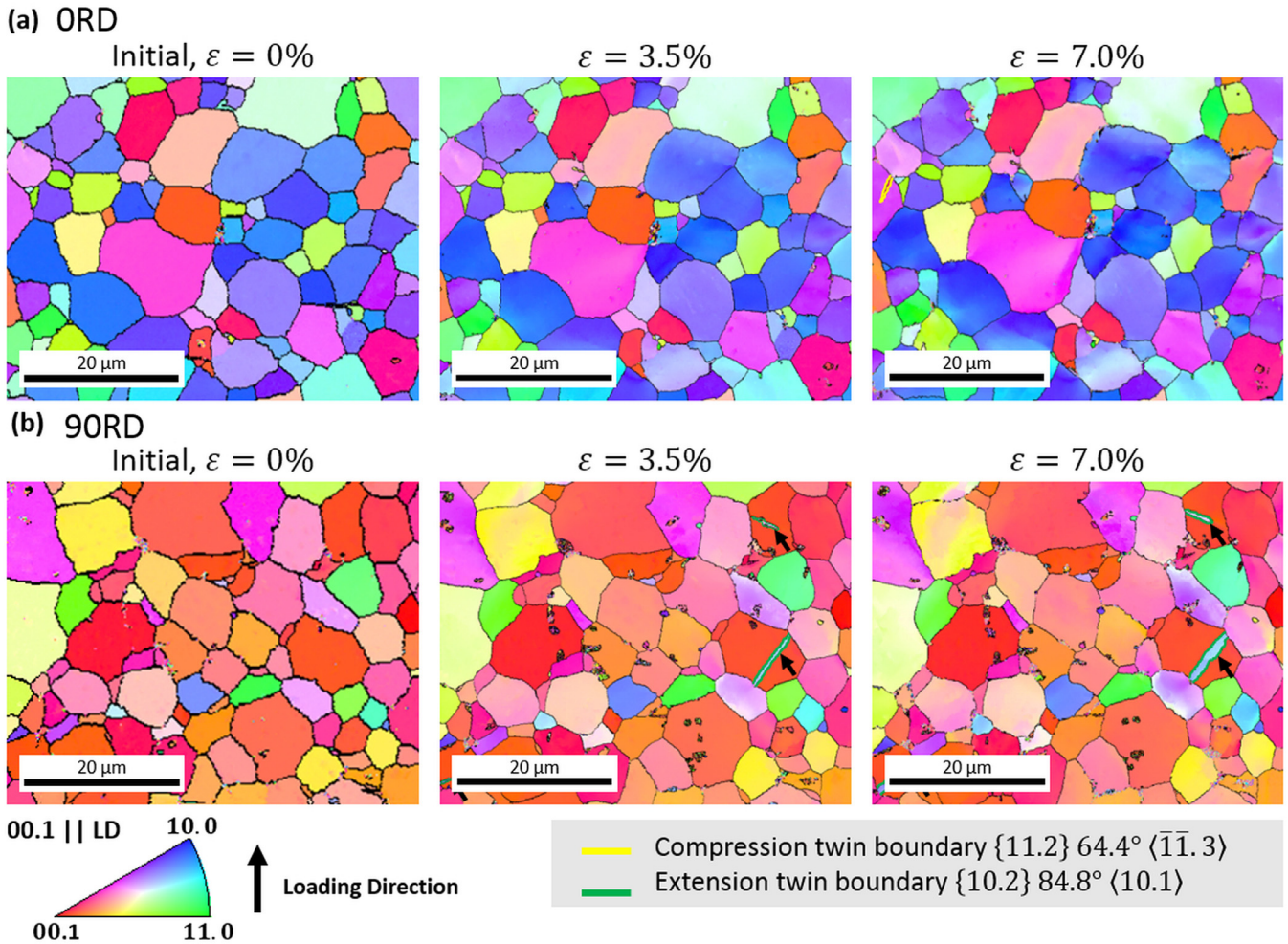
Fig. 5. Evolution of IPF grain orientation maps w.r.t. the loading direction for (a) 0RD and (b) 90RD sample. Dark spots on the strained 90RD samples are due to low confidence index areas.

broadening of the $(110)_{\parallel}\beta$ peak of a representative 0RD sample are available as supplementary material online.

Each axial α grain family consists of grains which all share the same orientation of the c-axis to the loading direction. Thus, the Schmid Factors (SFs) of the deformation mechanisms are the same for all of these grains. Conversely, each radial α grain family potentially consists of a wide range of grain orientations, *i.e.* contain plastically "soft" and "hard" grains. Therefore, the focus will primarily be on the lattice strain behavior of the axial grain families.

The relative integrated intensity evolution of the $(00.2)_{\parallel}\alpha$ and $\{10.0\}_{\parallel}\alpha$ grain families in a 90RD sample are shown in Fig. 7. The 90RD loading direction was chosen because it showed the largest amount of twinning during the quasi-*in situ* EBSD measurements. Error bars for these grain families were below 5% relative integrated intensity and are omitted for clarity. Around 0.0025 plastic strain, the $(00.2)_{\parallel}\alpha$ integrated intensity drops and the $\{10.0\}_{\parallel}\alpha$ integrated intensity rises. This is likely due to {10.2}-type tension twinning that was observed in the quasi-*in situ* EBSD. The integrated intensity then increases, which can be explained by grain rotation from dislocation slip which causes more grains to rotate into $(00.2)_{\parallel}\alpha$ Bragg condition. Between 385 and 390 MPa, the $(00.2)_{\parallel}\alpha$ integrated intensity drops suddenly again. This time, however, no corresponding increase is observed in the $\{10.0\}_{\parallel}\alpha$ intensity. This regime corresponds exactly to the $(00.2)_{\parallel}\alpha$ lattice strain drop observed in Fig. 6 and the last period in which the plastic work hardening is decreasing in Fig. 3(b). A gradual increase is then observed for both grain families until the end of the first

loading cycle, which can be explained by grain rotation due to dislocation slip.

The following can be deduced from the behavior of the peaks during the first loading cycle:

The elastic behavior (<150 MPa) of the axial grains depends on the grain family, showing that this material is elastically anisotropic. Grain orientations with the c-axis aligned along the loading direction behave elastically stiffer. This is consistent with the behavior of single crystal Ti, which has elastic lattice constants $E_{(2\bar{1}\bar{1}0)} = E_{(01\bar{1}0)} = 104$ MPa and $E_{(0001)} = 146.2$ MPa [59]. The spread of the elastic lattice strains increases as the angle from the rolling direction increases (Fig. 6).

For the 0RD samples (Fig. 6(a) and (b)), the $\{21.1\}_{\parallel}\alpha$ grain family sheds load around 150 MPa, implying that it plastifies well below the macroscopic yield stress. This can be explained by the activation of $Pri\langle a \rangle$ slip, the lowest-CRSS mechanism, as this grain family has the highest SF among the measured grain families (Fig. 2). There are only a small percentage of grains in this orientation, so the onset of microplasticity does not result in macroscopic yield. Instead, load is transferred to the plastically hard grain families, as seen for $(00.2)_{\parallel}\alpha$, $\{11.2\}_{\parallel}\alpha$, and $\{10.2\}_{\parallel}\alpha$. The $\{11.0\}_{\parallel}\alpha$, and $\{10.0\}_{\parallel}\alpha$ (not shown for clarity) shed load next, which can also be explained by the activation of $Pri\langle a \rangle$ slip. Due to the rolling texture, there are a large number of $\{11.0\}_{\parallel}\alpha$ and $\{10.0\}_{\parallel}\alpha$ grains (Fig. 1(a)) and the initiation of plasticity results in macroscopic yield. The soft grain families continue to take load after yield.
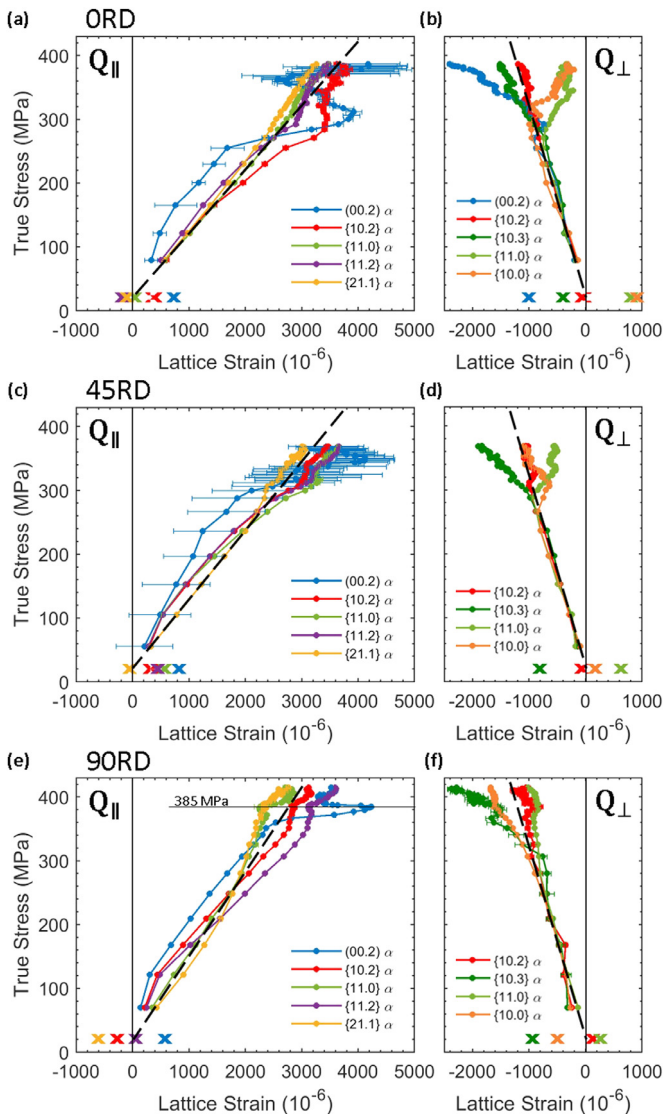
Fig. 6. Lattice strain evolution versus applied stress for (a, b) 0RD, (c, d) 45RD, and (e, f) 90RD samples. Selected axial ($\mathbf{Q}_\parallel$) and radial ($\mathbf{Q}_\perp$) α grain families are shown on the right and left, respectively. The unload of the lattice strain is linear for all grain families and is not shown for clarity. The residual lattice strains after unload are marked by "x".
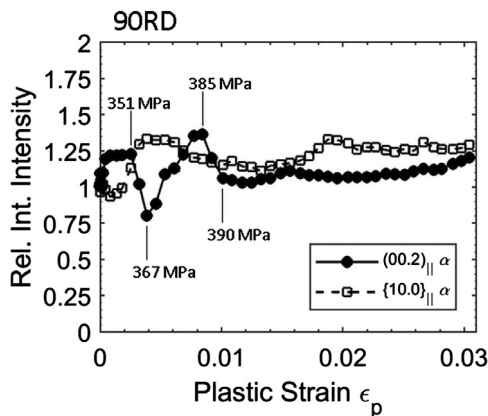

Fig. 7. Relative integrated intensity of the $(00.2)_\parallel$ α and $\{10.0\}_\parallel$ α grain families versus plastic strain during the first loading cycle for a 90RD sample.

At around 290 MPa, the $\{10.2\}_\parallel$ α and $\{11.2\}_\parallel$ α families shed load. The slope of the elastic lattice strain evolution for the $\{10.2\}_\parallel$ α grain family becomes nearly vertical, implying that they behave nearly perfect plastic upon yielding. The load is redistributed back to the softer grain families and the $(00.2)_\parallel$ α grains. SF analysis suggests that this is due to the initiation of $Ba\langle a\rangle$ slip in the $\{10.2\}_\parallel$ α and $\{11.2\}_\parallel$ α grain families.

At 310 MPa, the $(00.2)_\parallel$ α grain family begins to shed load. The SF for all $\langle a\rangle$-type slip mechanisms is 0, suggesting that this is due to the activation of $\langle c+a\rangle$ slip. At this point, all other grain families are taking load again. The elastic lattice strains in the $(00.2)_\parallel$ α family decrease, implying that the average stress on the grains must be decreasing. Since twinning only plays a small role in the deformation, the decrease must be related to instable plastic flow. However, as these grains are a minority due to the rolling texture, the lattice strain relaxation is not observed in the macroscopic mechanical response.

For the 45RD samples, the $\{21.1\}_\parallel$ α grain family behaves plastically soft, deforming well below macroplastic yield. Load is then redistributed to all of the other grain families as there is no strong texture along the loading axis. With the exception of the $(00.2)_\parallel$ α, all of the other grain families noticeably shed load at around 300 MPa, suggesting that plasticity initiates nearly simultaneously in many of the grains. All measured grain families behave nearly perfect plastic. This behavior explains the low plastic work hardening rate observed in Fig. 3(b). At around 335 MPa, the elastic lattice strains of the $(00.2)_\parallel$ α grain family suddenly drop. As in the 0RD sample, there is only a small percentage of grains in this orientation and the effect is not observed in the macroscopic response.

For the 90RD samples, the relative behavior of the grain families is similar to the 0RD samples. The plastically soft grain families (*e.g.* $\{21.1\}_\parallel$ α and $\{11.0\}_\parallel$ α) shed load early and the load is redistributed among the harder orientations. The $\{10.2\}_\parallel$ α and $\{11.2\}_\parallel$ α grain families behave nearly perfect plastic upon yield, and load is taken strongly by the $(00.2)_\parallel$ α grains. At this point, all of the measured grain families appear to be plastifying except the $(00.2)_\parallel$ α. Due to the rolling texture, there is a much larger percentage of plastically hard grain orientations in the 90RD samples, resulting in the highest yield stress. Between 385 and 390 MPa, the elastic lattice strains of the $(00.2)_\parallel$ α grain family drop sharply as the family plastifies. Load is redistributed to all of the other grain families. This stress range corresponds to the work hardening plateau highlighted in Fig. 3(b), where the plastic work hardening rate is lower than the other two directions. After 390 MPa, the $(00.2)_\parallel$ α grain family begins to take load again, implying that the grains have hardened.

The effect of the texture differences between 0RD, 45RD, and 90RD can also be seen in the evolution of the radial $\{10.0\}_\perp$ α elastic lattice strains. This grain family consists of a range of grain orientations with *c*-axis between 0° and 90° to the loading axis. Due to the rolling texture, the proportion of grains in each orientation is different depending on the loading direction. In the 0RD samples (Fig. 6(b)), the majority of the $\{10.0\}_\perp$ α grains are perpendicular to the loading axis and have a soft orientation with SF > 0.37 for low-CRSS $Pri\langle a\rangle$. The grain family sheds load strongly. In the 90RD samples (Fig. 6(f)), the majority of the grains have their *c*-axis nearly parallel to the loading direction, a hard orientation which deforms by high-CRSS $\langle c+a\rangle$ slip. Consequently, the grain family behaves plastically hard and takes load.

3.3.2. Peak profile evolution

Williamson Hall (WH) plots for the three loading directions are shown in Fig. 8. The samples are the same as the ones used for the lattice strain evolution. The peak broadening between the initial (unloaded) state and the fully loaded state after $\varepsilon = 10.5\%$ are
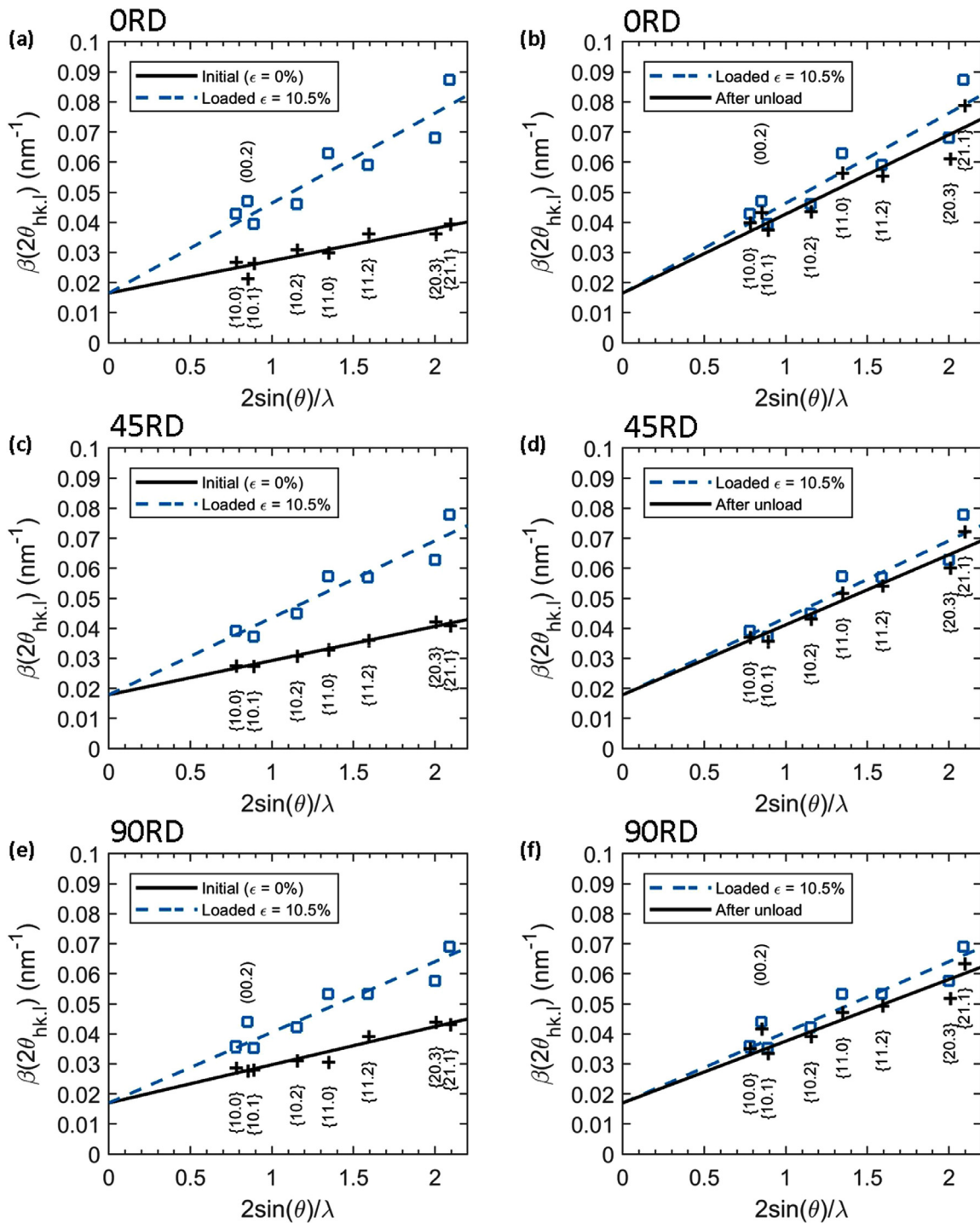
Fig. 8. Williamson Hall (W–H) plots for the (a, b) 0RD, (c, d) 45RD, and (e, f) 90RD samples. The left column shows the W–H plots for the initial (unloaded) microstructure and after the third load to 10.5% macroscopic strain. The right column shows the W–H plots after the third load and after the third unload.

shown in Fig. 8(a), (c), and (e). The peak width decreases from this loaded state to the fully unloaded state (*i.e.* the third unload) are shown in Fig. 8(b), (d), and (f). Error bars were too small to be visible on the graphs. The peak broadening is shown only for the third load cycle for clarity. However, the peak broadening trends observed in Fig. 8 are consistent across all three load and unload cycles. The W–H plots for the first and second load–unload cycles can be found online as supplementary material.

The non-zero slope of the linear regression in the initial state of all samples indicates that inhomogeneous residual strain is present

in the initial microstructure. Upon straining, the slope of the regression line increases, indicating that the inhomogeneous elastic strain is increasing. For the same macroscopic strain increment, the 0RD shows the largest increase in inhomogeneous elastic strain while the 90RD sample shows the lowest. The same trends are observed for each grain family across the three loading directions. The $\{10.0\}_{\parallel}\,\alpha$, $\{11.0\}_{\parallel}\,\alpha$, $\{2.11\}_{\parallel}\,\alpha$, and $(00.2)_{\parallel}\,\alpha$ grain families generally rise further above the line, while the $\{10.1\}_{\parallel}\,\alpha$, $\{10.2\}_{\parallel}\,\alpha$, $\{11.2\}_{\parallel}\,\alpha$, and $\{20.3\}_{\parallel}\,\alpha$ families fall further below the line with each increase in macroscopic strain. This behavior is
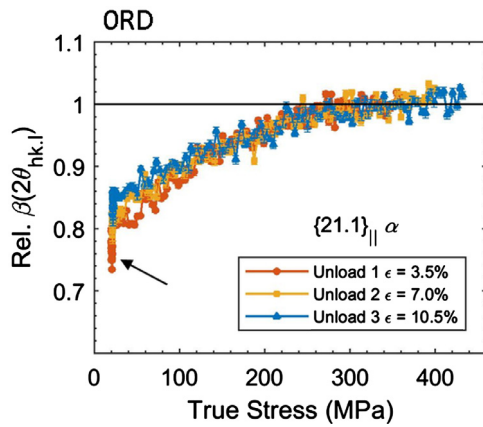
Fig. 9. Relative $\beta(2\theta_{hk.l})$ evolution of the $\{11.2\}_\parallel$ α grain family of the 0RD sample during each unloading. The $\beta(2\theta_{hk.l})$ is normalized to the average value of the measurements above 300 MPa. The arrow highlights the continued decrease in peak width after the sample is unloaded.

difficult to interpret as the peak broadening depends on the dislocation density and the contrast factor of each grain family [55,60], which requires large assumptions about the active slip systems and nature of the dislocations (screw or edge) in the grain family. However, the relatively large increase in $\beta(2\theta_{hk.l})$ of the $(00.2)_\parallel$ α grain family is perhaps expected. The SF for $\langle a \rangle$-type slip mechanisms is 0, so the majority of strain should be accommodated by $Pyr^{1st} \langle c + a \rangle$ slip. The activity of this mechanism has a relatively large contrast factor for $(00.2)_\parallel$ grains, which would result in the large observed peak broadening.

Regardless of loading direction, the unloads along the 0RD direction consistently show a larger slope decrease. This is consistent with the larger anelastic strain recovery observed in the 0RD samples compared to the 45RD and 90RD samples. All grain families show a decrease in peak width and maintain their relative position with respect to the regression line.

The relative $\beta(2\theta_{hk.l})$ evolution during the unloads of the $\{11.2\}_\parallel$ α grain family in the 0RD sample is shown in Fig. 9. The values of $\beta(2\theta_{hk.l})$ were normalized to the average value of the measurements above 300 MPa. This grain family was chosen because it clearly shows the non-linear decrease in peak width observed in all grain families. The rate at which $\beta(2\theta_{hk.l})$ decreases changes noticeably between 250 and 300 MPa for all grain families, the same stress range where the macroscopic unload begins to deviate noticeably from the elastic component of the unload (Fig. 3(d)). The $\beta(2\theta_{hk.l})$ evolution is consistent regardless of pre-strain and always begins at the same stress. After each unload, the samples were held constant at 20 MPa for 5 min. The peak width continues to decrease during the hold, highlighted by an arrow in Fig. 9.

4. Discussion

4.1. Three-stage work hardening

A work hardening plateau is observed during loading along 90RD (Fig. 3(b)). This behavior is often described during compression for CP-Ti [24–28] and other HCP materials [29–32] as the result of $\{10.2\}\langle10.1\rangle$ tension twinning and the subsequent hardening in which dislocation glide is hindered by the new twin boundaries. More recently, the three-stage work hardening has been reported for tensile tests in CP-Ti [1–3]. Becker and Pantleon [2] reported that the three stages correspond to easy dislocation slip, the activation of $\{11.2\}\langle\bar{1}\bar{1}.3\rangle$ compression twinning, and the saturation of this twinning system and subsequent activation of

$\{10.2\}\langle10.1\rangle$ tension twinning. On the other hand, both Roth et al. [1] and Amouzou et al. [3] observed almost no twinning ($<0.5\%$ and 5.7 vol%. fraction for rolling direction and transverse direction samples, respectively) and thus proposed that the work hardening plateau is the result of multi-slip work hardening after an initial period of easy single glide.

Only a small fraction of deformation twinning is observed by quasi-*in situ* EBSD, and the integrated intensity evolution in Fig. 7 suggests that deformation twinning occurs before the work hardening plateau. This supports the idea that the three-stage work hardening is predominantly governed by dislocation-based mechanisms. A minimum is observed in the plastic work hardening rate of the 90RD samples at around $\varepsilon_p = 0.01$ (an applied stress of 390 MPa). This occurs just after a sudden lattice strain relaxation in the $(00.2)_\parallel$ α grain family that can be rationalized by the activation and rapid multiplication of $Pyr^{1st} \langle c + a \rangle$ slip. In fact, this behavior is observed for all loading directions but only noticeably affects the macroscopic response of the 90RD sample due to the large percentage of $(00.2)_\parallel$ α grains. As the $(00.2)_\parallel$ α grain family plastifies, load is redistributed to the other grain families. These observations are supported by the EVPSC model of Richeton et al. [48], which predicts that the low initial work hardening rate can be explained by a reduction in intergranular stresses and the fast multiplication of mobile $Pyr^{1st} \langle c + a \rangle$ dislocations. The easy generation and glide of dislocations in the $(00.2)_\parallel$ α grains is rapidly exhausted and the grains begin to harden. The plastic work hardening rate increases. Once the $(00.2)_\parallel$ α grains harden sufficiently they again behave plastically hard. Plastic flow increases in the other grain families and the work hardening rate begins to decrease in parallel with the 0RD and 45RD samples.

The elastic lattice strain drop of the $(00.2)_\parallel$ α grain family also gives direct evidence that the grain-resolved stress along the loading direction decreases in grains during continuous loading. This was recently reported for the first time in CP Ti by Abdolvand et al. [23], who observed the phenomenon in several grains with 3D-XRD. They also performed crystal plasticity finite element simulations which suggest that the stress drop is largest in plastically hard grains surrounded by hard grain neighbors. This is consistent with the much quicker lattice strain relaxation observed in the 90RD samples, as this type of hard grain "cluster" should be more prevalent due to the rolling texture. However, the presence of the lattice strain drop in all samples suggests that this effect is active regardless of loading direction.

4.2. Non-linear anelastic strain recovery

A non-linear springback is observed during unloading for all loading directions. Khayatzadeh et al. [8,9] previously described the springback in the same material as the cumulative effect of three components: the elastic recovery, a degradation in the elastic modulus, and an anelastic strain recovery. No degradation in the elastic modulus was observed in our results, although the initial springback behavior was likely affected by the slow reversal of the machine crosshead. However, an anelastic strain recovery was observed to occur for all loading directions. Consistent with the findings of Khayatzadeh et al., the anelastic strain recovery is larger along 0RD than in 45RD and 90RD and appears to stay constant regardless of pre-strain (Fig. 4).

The unloading behavior may be explained by anelastic effects. Described by Zener and Siegel [61], anelastic deformation is driven by local internal sources of stress, such as dislocation pile-ups. As the applied load is decreased, these backstresses overcome the forward stress and drive mobile dislocations backward. The peak width begins to decrease, suggesting that dislocations are either annihilating or rearranging to reduce the strain. Between 250 and 300 MPa (depending on the grain family), the peak width for all

grain families starts to decrease more quickly. Consequently, the anelastic strain recovery begins to increase exponentially. Cleveland and Ghosh [13] describe this regime as the release of dislocations that were initially pinned in the forward direction. As the forward applied stress is reduced, progressively more dislocations reach the critical stress for backwards motion. A higher number of dislocations increases the likelihood of annihilation events, resulting in the exponential decrease in $\beta(2\theta_{hk.l})$.

The presence of strong residual backstresses results in the continued decrease in *FWHM* even as the sample is held constant in the "unloaded" state (20 MPa). The backstresses continue to drive dislocation annihilation and result in the continued decrease in macroscopic strain even as the same is held in the unloaded state. This description is consistent with studies on time-dependent plastic strain recovery reported in aluminum alloys and steels [13,62–64].

The observed springback anisotropy implies that the internal stress does not develop equally along the different loading directions. This is visible in the W–H plots, which show that the inhomogeneous elastic strain increases more quickly with macroscopic strain along the rolling direction. The elastic lattice strain evolutions also show that the residual stress state varies with loading direction. In the 0RD sample, the majority of grains lie with their *c*-axis oriented near perpendicular to the loading direction. The behavior of the $\{10.0\}_{\parallel}\alpha$, $\{11.0\}_{\parallel}\alpha$, and $\{21.1\}_{\parallel}\alpha$ grain families suggest that these grains will end with approximately no residual stress. By parallel logic, the behavior of the $(00.2)_{\parallel}\alpha$ grain family suggest that majority of grains in the 90RD sample will end up with a tensile residual stress along the loading direction. The larger anelastic springback along the rolling direction can thus be explained by the (1) larger number of grains with low-CRSS dislocations and (2) presence of stronger backstresses to push these dislocations backwards along the loading direction.

Despite being a backstress-driven process, the anelastic component of the springback does not appear to increase with increasing pre-strain, and the non-linear behavior consistently starts in the same stress range. This implies that, despite an increase in the dislocation density with additional macroscopic strain, the backwards mobile dislocation density saturates within the first 3.5% of macroscopic strain. This can be explained by a competition between higher backstresses and a lower mean free path of the mobile dislocations, both caused by the increasing dislocation density.

5. Conclusion

The deformation behavior of cold-rolled CP Ti sheet was examined by *in situ* XRD, quasi-*in situ* EBSD, and HRDIC. The material exhibits a three-stage work hardening during tensile loading despite the lack of significant twin activity. The work hardening plateau is shown to be the result of the sudden activation and multiplication of $\langle c + a \rangle$ slip in plastically hard grains which results in redistribution of load among other grain families. A non-linear anelastic springback is observed during unloading that can be attributed to the annihilation/rearrangement of dislocations. XRD measurements imply the development of higher internal stresses during loading in the rolling direction, resulting in a significant springback anisotropy. These results can be used to improve crystal plasticity simulations for the prediction of tensile deformation and springback behavior in Ti.

Acknowledgments

Supplementary materials

Supplementary material associated with this article can be found, in the online version, at doi:10.1016/j.actamat.2019.09.039.

References

[1] A. Roth, M.A. Lebyodkin, T.A. Lebedkina, J.-S. Lecomte, T. Richeton, K.E.K. Amouzou, Mechanisms of anisotropy of mechanical properties of α-titanium in tension conditions, Mater. Sci. Eng. A 596 (2014) 236–243, doi:10.1016/j.msea.2013.12.061.

[2] H. Becker, W. Pantleon, Work-hardening stages and deformation mechanism maps during tensile deformation of commercially pure titanium, Comput. Mater. Sci. 76 (2013) 52–59, doi:10.1016/j.commatsci.2013.03.028.

[3] K.E.K. Amouzou, T. Richeton, A. Roth, M.A. Lebyodkin, T.A. Lebedkina, Micromechanical modeling of hardening mechanisms in commercially pure α-titanium in tensile condition, Int. J. Plast. 80 (2016) 222–240, doi:10.1016/j.ijplas.2015.09.008.

[4] T. Hama, T. Sakai, Y.P. Korkolis, H. Takuda, Crystal-plasticity finite-element simulation of time-dependent springback in a commercially-pure titanium sheet, J. Phys. Conf. Ser. 1063 (2018) 012122, doi:10.1088/1742-6596/1063/1/012122.

[5] O.M. Badr, B. Rolfe, P. Zhang, M. Weiss, Applying a new constitutive model to analyse the springback behaviour of titanium in bending and roll forming, Int. J. Mech. Sci. 128–129 (2017) 389–400, doi:10.1016/j.ijmecsci.2017.05.025.

[6] Y.X. Zhu, Y.L. Liu, H. Yang, H.P. Li, Development and application of the material constitutive model in springback prediction of cold-bending, Mater Des. 42 (2012) 245–258, doi:10.1016/j.matdes.2012.05.043.

[7] L. Luo, A.K. Ghosh, Elastic and inelastic recovery after plastic deformation of DQSK steel sheet, J. Eng. Mater. Technol. 125 (3) (2003) 237–246, doi:10.1115/1.1491574.

[8] S. Khayatzadeh, S. Rahimi, P. Blackwell, Effect of plastic deformation on elastic and plastic recovery in CP-titanium, Key Eng. Mater. 716 (2016) 891–896, doi:10.4028/www.scientific.net/KEM.716.891.

[9] S. Khayatzadeh, M.J. Thomas, Y. Millet, S. Rahimi, Characterisation and modeling of in-plane springback in a commercially pure titanium (CP-Ti), J. Mater. Sci. 53 (9) (2018) 6872–6892, doi:10.1007/s10853-017-1983-8.

[10] J. Mendiguren, F. Cortés, X. Gómez, L. Galdos, Elastic behavior characterisation of TRIP 700 steel by means of loading–unloading tests, Mater. Sci. Eng. A 634 (2015) 147–152, doi:10.1016/j.msea.2015.03.050.

[11] Z. Chen, U. Gandhi, J. Lee, R.H. Wagoner, Variation and consistency of Young's modulus in steel, J. Mater. Process. Technol. 227 (2016) 227–243, doi:10.1016/j.jmatprotec.2015.08.024.

[12] J.A. Benito, J. Jorba, J.M. Manero, A. Roca, Change of Young's modulus of cold-deformed pure iron in a tensile test, Metall. Mater. Trans. A 36 (12) (2005) 3317–3324, doi:10.1007/s11661-005-0006-6.

[13] R.M. Cleveland, A.K. Ghosh, Inelastic effects on springback in metals, Int. J. Plast. 18 (5–6) (2002) 769–785, doi:10.1016/S0749-6419(01)00054-7.

[14] F. Morestin, M. Boivin, On the necessity of taking into account the variation in the Young modulus with plastic strain in elastic-plastic software, Nucl. Eng. Des. 162 (1) (1996) 107–116, doi:10.1016/0029-5493(95)01123-4.

[15] M. Yang, Y. Akiyama, T. Sasaki, Evaluation of change in material properties due to plastic deformation, J. Mater. Process. Technol. 151 (1–3) (2004) 232–236, doi:10.1016/j.jmatprotec.2004.04.114.

[16] R. Pérez, J.A. Benito, J.M. Prado, Study of the inelastic response of trip steels after plastic deformation, ISIJ Int. 45 (12) (2005) 1925–1933, doi:10.2355/isijinternational.45.1925.

[17] H.Y. Yu, Variation of elastic modulus during plastic deformation and its influence on springback, Mater. Des. 30 (3) (2009) 846–850, doi:10.1016/j.matdes.2008.05.064.

[18] L. Sun, R.H. Wagoner, Complex unloading behavior: nature of the deformation and its consistent constitutive representation, Int. J. Plast. 27 (7) (2011) 1126–1144, doi:10.1016/j.ijplas.2010.12.003.

[19] D. Shechtman, D.G. Brandon, Orientation dependent slip in polycrystalline titanium, J. Mater. Sci. 8 (9) (1973) 1233–1237, doi:10.1007/BF00549337.

[20] S. Han, P. Eisenlohr, M.A. Crimp, ECCI based characterization of dislocation shear in polycrystalline arrays during heterogeneous deformation of commercially pure titanium, Mater. Charact. 142 (2018) 504–514, doi:10.1016/j.matchar.2018.06.003.

[21] C.H. Cáceres, T. Sumitomo, M. Veidt, Pseudoelastic behavior of cast magnesium AZ91 alloy under cyclic loading–unloading, Acta Mater. 51 (20) (2003) 6211–6218, doi:10.1016/S1359-6454(03)00444-0.

[22] T. Hama, Y. Tanaka, M. Uratani, H. Takuda, Deformation behavior upon two-step loading in a magnesium alloy sheet, Int. J. Plast. 82 (2016) 283–304, doi:10.1016/j.ijplas.2016.03.009.

[23] H. Abdolvand, J. Wright, A.J. Wilkinson, Strong grain neighbour effects in polycrystals, Nat. Commun. 9 (1) (2018) 171, doi:10.1038/s41467-017-02213-9.

[24] S. Nemat-Nasser, W.G. Guo, J.Y. Cheng, Mechanical properties and deformation mechanisms of a commercially pure titanium, Acta Mater. 47 (13) (1999) 3705–3720, doi:10.1016/S1359-6454(99)00203-7.

K. Sofinowski, M. Šmíd and S. van Petegem et al. / Acta Materialia 181 (2019) 87–98

[25] A.A. Salem, S.R. Kalidindi, R.D. Doherty, Strain hardening regimes and microstructure evolution during large strain compression of high purity titanium, Scr. Mater. 46 (6) (2002) 419–423, doi:10.1016/S1359-6462(02)00005-2.

[26] A.A. Salem, S.R. Kalidindi, R.D. Doherty, Strain hardening of titanium: role of deformation twinning, Acta Mater. 51 (14) (2003) 4225–4237, doi:10.1016/S1359-6454(03)00239-8.

[27] A.A. Salem, S.R. Kalidindi, R.D. Doherty, S.L. Semiatin, Strain hardening due to deformation twinning in α-titanium: mechanisms, Metall. Mater. Trans. A 37 (1) (2006) 259–268, doi:10.1007/s11661-006-0171-2.

[28] F. Coghe, W. Tirry, L. Rabet, D. Schryvers, P. van Houtte, Importance of twinning in static and dynamic compression of a Ti–6Al–4V titanium alloy with an equiaxed microstructure, Mater. Sci. Eng. A 537 (2012) 1–10, doi:10.1016/j.msea.2011.12.047.

[29] L. Jiang, J.J. Jonas, R.K. Mishra, A.A. Luo, A.K. Sachdev, S. Godet, Twinning and texture development in two Mg alloys subjected to loading along three different strain paths, Acta Mater. 55 (11) (2007) 3899–3910, doi:10.1016/j.actamat.2007.03.006.

[30] M.R. Barnett, Z. Keshavarz, A.G. Beer, D. Atwell, Influence of grain size on the compressive deformation of wrought Mg–3Al–1Zn, Acta Mater. 52 (17) (2004) 5093–5103, doi:10.1016/j.actamat.2004.07.015.

[31] D. Sarker, D.L. Chen, Detwinning and strain hardening of an extruded magnesium alloy during compression, Scr. Mater. 67 (2) (2012) 165–168, doi:10.1016/j.scriptamat.2012.04.007.

[32] B. Wang, R. Xin, G. Huang, Q. Liu, Effect of crystal orientation on the mechanical properties and strain hardening behavior of magnesium alloy AZ31 during uniaxial compression, Mater. Sci. Eng. A 534 (2012) 588–593, doi:10.1016/j.msea.2011.12.013.

[33] M. Drakopoulos, T. Connolley, C. Reinhard, R. Atwood, O. Magdysyuk, N. Vo, M. Hart, L. Connor, B. Humphreys, G. Howell, S. Davies, T. Hill, G. Wilkin, U. Pedersen, A. Foster, N. De Maio, M. Basham, F. Yuan, K. Wanelik, I12: the Joint Engineering, Environment and Processing (JEEP) beamline at diamond light source, J. Synchrotron Rad. 22 (3) (2015) 828–838, doi:10.1107/S1600577515003513.

[34] J. Filik, A.W. Ashton, P.C.Y. Chang, P.A. Chater, S.J. Day, M. Drakopoulos, M.W. Gerring, M.L. Hart, O.V. Magdysyuk, S. Michalik, A. Smith, C.C. Tang, N.J. Terrill, M.T. Wharmby, H. Wilhelm, Processing two-dimensional X-ray diffraction and small-angle scattering data in DAWN 2, J. Appl. Cryst. 50 (3) (2017) 959–966, doi:10.1107/S1600576717004708.

[35] O. Muránsky, D.G. Carr, M.R. Barnett, E.C. Oliver, P. Šittner, Investigation of deformation mechanisms involved in the plasticity of AZ31 Mg alloy: in situ neutron diffraction and EPSC modelling, Mater. Sci. Eng. A 496 (1–2) (2008) 14–24, doi:10.1016/j.msea.2008.07.031.

[36] S.R. Agnew, D.W. Brown, C.N. Tomé, Validating a polycrystal model for the elastoplastic response of magnesium alloy AZ31 using in situ neutron diffraction, Acta Mater. 54 (18) (2006) 4841–4852, doi:10.1016/j.actamat.2006.06.020.

[37] K. Sofinowski, T. Panzner, M. Kubenova, J. Čapek, S. van Petegem, H. van Swygenhoven, In situ tension-tension strain path changes of cold-rolled Mg AZ31B, Acta Mater. 164 (2019) 135–152, doi:10.1016/j.actamat.2018.10.033.

[38] B. Clausen, T. Lorentzen, T. Leffers, Self-consistent modeling of the plastic deformation of f.c.c. polycrystals and its implications for diffraction measurements of internal stresses, Acta Mater. 46 (9) (1998) 3087–3098, doi:10.1016/S1359-6454(98)00014-7.

[39] F. Bachmann, R. Hielscher, H. Schaeben, Texture analysis with MTEX – free and open source software toolbox, Solid State Phenom. 160 (2010) 63–68, doi:10.4028/www.scientific.net/SSP.160.63.

[40] B. Barkia, V. Doquet, J.P. Couzinié, I. Guillot, E. Héripré, In situ monitoring of the deformation mechanisms in titanium with different oxygen contents, Mater. Sci. Eng, A 636 (2015) 91–102, doi:10.1016/j.msea.2015.03.044.

[41] J. Gong, A.J. Wilkinson, Anisotropy in the plastic flow properties of single-crystal α titanium determined from micro-cantilever beams, Acta Mater. 57 (19) (2009) 5693–5705, doi:10.1016/j.actamat.2009.07.064.

[42] C. Zambaldi, Y. Yang, T.R. Bieler, D. Raabe, Orientation informed nanoindentation of α-titanium: indentation pileup in hexagonal metals deforming by prismatic slip, J. Mater. Res. 27 (1) (2012) 356–367, doi:10.1557/jmr.2011.334.

[43] M.J. Philippe, M. Serghat, P. van Houtte, C. Esling, Modeling of texture evolution for materials of hexagonal symmetry—II. Application to zirconium and

[44] titanium α or near α alloys, Acta Metall. Mater. 43 (4) (1995) 1619–1630, doi:10.1016/0956-7151(94)00329-G.

[44] N.P. Gurao, R. Kapoor, S. Suwas, Deformation behaviour of commercially pure titanium at extreme strain rates, Acta Mater. 59 (9) (2011) 3431–3446, doi:10.1016/j.actamat.2011.02.018.

[45] J.L.W. Warwick, N.G. Jones, K.M. Rahman, D. Dye, Lattice strain evolution during tensile and compressive loading of CP Ti, Acta Mater. 60 (19) (2012) 6720–6731, doi:10.1016/j.actamat.2012.08.042.

[46] N. Benmhenni, S. Bouvier, R. Brenner, T. Chauveau, B. Bacroix, Micromechanical modelling of monotonic loading of CP α-Ti: correlation between macroscopic and microscopic behaviour, Mater. Sci. Eng. A 573 (2013) 222–233, doi:10.1016/j.msea.2013.02.022.

[47] D. Gloaguen, G. Oum, V. Legrand, J. Fajoui, S. Branchu, Experimental and theoretical studies of intergranular strain in an alpha titanium alloy during plastic deformation, Acta Mater. 61 (15) (2013) 5779–5790, doi:10.1016/j.actamat.2013.06.022.

[48] T. Richeton, F. Wagner, C. Chen, L.S. Toth, Combined effects of texture and grain size distribution on the tensile behavior of α-titanium, Materials 11 (7) (2018) 1088, doi:10.3390/ma11071088.

[49] H. Conrad, Effect of interstitial solutes on the strength and ductility of titanium, Prog. Mater. Sci. 26 (2–4) (1981) 123–403, doi:10.1016/0079-6425(81)90001-3.

[50] T. Xiaoli, G. Haicheng, Z. Shufen, C. Laird, Loading mode dependence of deformation microstructure in a high-purity titanium single crystal oriented for difficult glide, Mater. Sci. Eng. A 189 (1–2) (1994) 77–84, doi:10.1016/0921-5093(94)90403-0.

[51] C.E. Krill, in: U.d. Saarlandes (Ed.), A Short Polemic on Crystallite Size/strain Determination Using X-ray Diffraction, 1994.

[52] A.L. Patterson, The Scherrer formula for X-ray particle size determination, Phys. Rev. 56 (10) (1939) 978–982, doi:10.1103/PhysRev.56.978.

[53] A.R. Stokes, A.J.C. Wilson, A method of calculating the integral breadths of Debye–Scherrer lines, Math. Proc. Camb. Philos. Soc. 38 (2) (1942) 313–322, doi:10.1017/S0305004100021988.

[54] G.K. Williamson, W.H. Hall, X-ray line broadening from filed aluminium and wolfram, Acta Metall. 1 (1) (1953) 22–31, doi:10.1016/0001-6160(53)90006-6.

[55] I.C. Dragomir, T. Ungár, Contrast factors of dislocations in the hexagonal crystal system, J. Appl. Cryst. 35 (5) (2002) 556–564, doi:10.1107/S0021889802009536.

[56] T. Ungár, Á. RRévész, A. Borbély, Dislocations and grain size in electrodeposited nanocrystalline Ni determined by the modified Williamson–Hall and Warren–Averbach procedures, J. Appl. Cryst. 31 (4) (1998) 554–558, doi:10.1107/S0021889897019559.

[57] T. Ungár, A. Borbély, The effect of dislocation contrast on x-ray line broadening: a new approach to line profile analysis, Appl. Phys. Lett. 69 (21) (1996) 3173–3175, doi:10.1063/1.117951.

[58] H. van Swygenhoven, B. Schmitt, P.M. Derlet, S. van Petegem, A. Cervellino, Z. Budrovic, S. Brandstetter, A. Bollhalder, M. Schild, Following peak profiles during elastic and plastic deformation: a synchrotron-based technique, Rev. Sci. Instrum. 77 (1) (2006) 013902, doi:10.1063/1.2162453.

[59] D. Tromans, Elastic anisotropy of HCP metal crystals and polycrystals, Int. J. Recent Res. Appl. Stud. 6 (2011) 462–483.

[60] T.H. Simm, Peak broadening anisotropy and the contrast factor in metal alloys, Crystals 8 (5) (2018) 212, doi:10.3390/cryst8050212.

[61] C.M. Zener, S. Siegel, Elasticity and anelasticity of metals, J. Phys. Chem. 53 (9) (1949) 1468–1468, doi:10.1021/j150474a017.

[62] H. Lim, M.G. Lee, J.H. Sung, J.H. Kim, R.H. Wagoner, Time-dependent springback of advanced high strength steels, Int. J. Plast. 29 (2012) 42–59, doi:10.1016/j.ijplas.2011.07.008.

[63] J. Wang, R.H. Wagoner, W.D. Carden, D. Matlock, F. Barlat, Creep and anelasticity in the springback of aluminum, Int. J. Plast. 20 (12) (2004) 2209–2232, doi:10.1016/j.ijplas.2004.05.008.

[64] H. Kim, C. Kim, F. Barlat, E. Pavlina, M.-.G. Lee, Nonlinear elastic behaviors of low and high strength steels in unloading and reloading, Mater. Sci. Eng. A 562 (2013) 161–171, doi:10.1016/j.msea.2012.11.020.